Title: Tumor cell heterogeneity drives spatial organization of the intratumoral immune response in squamous cell skin carcinoma

Authors:

Miho Tanaka[1], Lotus Lum[1], Kenneth Hu[2], Cecilia Ledezma-Soto[1], Daphne Superville[1], Kenneth Ng[1], Zoe Adams[1], Kelly Kersten[2], Lawrence Fong[3], Matthew Krummel[2], Melissa Reeves[4]

Affiliations:

[1]Department of Microbiology and Immunology, University of California, San Francisco

[2]Department of Pathology, University of California, San Francisco

[3]Deparment of Medicine, University of California, San Francisco

[4]The Huntsman Cancer Institute & Department of Pathology, University of Utah

Keywords:

Intratumoral heterogeneity, tumor immune microenvironment, immune checkpoint blockade, spatial immune heterogeneity

Abstract:

Intratumoral heterogeneity (ITH)—defined as genetic and cellular diversity within a tumor—is linked to a failure of immunotherapy in multiple cancer types and to an inferior anti-tumor immune response even in the absence of therapy. To determine how tumor heterogeneity shapes the immune microenvironment and impacts responses to therapy, we modeled

23 heterogeneous tumors comprised of a pro-inflammatory (“hot”) and an immunosuppressive
24 (“cold”) tumor population. This was done by mixing two squamous skin carcinoma cell lines that
25 alone give rise to tumors with a reproducible immunologically “hot” or “cold” immune
26 phenotype respectively, and labeling these with YFP or RFP fluorescent tags to enable precise
27 spatial tracking. The resulting mixed-population tumors were made up of a patchwork of
28 distinct regions that could be classified as being comprised of YFP^+ (“hot”) cells, RFP^+ (“cold”)
29 cells, or a mixture of YFP^+ and RFP^+ cells. We find the spatial organization of tumor cells creates
30 a blueprint for the spatial organization and functional activity of infiltrating immune cells,
31 defining the architecture of both tumor-infiltrating T cell and myeloid cell compartments. Using
32 a combination of microdissection techniques and single-cell spatial transcriptomics, we show
33 that YFP regions harbor a higher frequency of Th1 cells and $IFN\gamma^+$ CD8 T cells compared to RFP
34 regions, whereas immunosuppressive macrophages preferentially accumulate in RFP regions.
35 Total CD4 T cells were also enriched in YFP regions, but by contrast, total CD8 T cells—despite
36 their superior function in YFP regions—were of low abundance throughout the heterogeneous
37 tumors. We identify the chemokine Cx3cl1, produced at higher levels by our “cold” tumors, as a
38 mediator of intratumoral macrophage abundance, and show that overexpression of Cx3cl1 in
39 pro-inflammatory (“hot”) tumor cells leads to an increase in immunosuppressive $CD206^{Hi}$
40 macrophages. We further interrogated the impact of this spatial patterning of immune cells on
41 the responses of heterogeneous tumors to checkpoint blockade. We find that combination of
42 PD-1 blockade and CD40 agonist is able to increase the Th1 response in “cold” RFP regions,
43 however the T cell response in “cold” regions remains inferior to “hot” regions and treatment
44 achieves only a modest reduction in tumor growth. Collectively, our results demonstrate that

45 the spatial organization of heterogeneous tumor cells has a profound impact on directing the
46 spatial organization and function of tumor-infiltrating immune cells as well as on responses to
47 immunotherapy.
48
49
50 **Introduction:**
51 Immunotherapies have shown great promise in treating cancer by activating a patient's
52 own immune cells to fight their tumor, but only a fraction of patients respond to current
53 treatment regimens[1–4]. Immune checkpoint blockade (ICB) therapy routinely achieves durable
54 cures in only a limited number of cancer types, and in many tumor types, response rates are as
55 low as 15% with high relapse rates[3,4]. Genetic heterogeneity within a tumor is a significant
56 factor that has been linked to poor ICB response[5–7]. Tumors are often comprised of multiple
57 populations of cancer cells, with each population carrying a distinct set of genetic alterations
58 and phenotypic behaviors[8–10]. Genetic heterogeneity—often given the generalized label
59 "intratumoral heterogeneity" (ITH)—is inherent in all cancer types[6], and studies in multiple
60 cancer types have shown that tumors with high genetic heterogeneity (high ITH) are less likely
61 to respond to ICB regimens[5,7]. Further, in patients, tumors are frequently a patchwork of "hot"
62 and "cold" regions[11–13]—characterized by high and low T cell infiltrates, respectively —
63 indicating that a dysfunctional T cell phenotype can be spatially localized. One study of 85 pre-
64 treatment lung cancers revealed that over two-thirds of tumors investigated contained both
65 "hot" and "cold" regions[11]. However, model systems that lend themselves to mechanistically

66 interrogating the impact of tumor heterogeneity on the spatial organization of immune cells
67 within a tumor are limited at present.

68 Heterogeneity-induced impairment of the anti-tumor immune response has also been
69 observed in mouse models[14–16]. A mixture of two mouse pancreatic ductal adenocarcinoma
70 (PDAC) cell lines, one giving rise to “immune hot” and the other to “immune cold” tumors on its
71 own, resulted in an overall “cold” tumor, suggesting that “coldness” may be a dominant
72 phenotype[14]. Another study in a murine melanoma model showed that high-heterogeneity
73 tumors exhibited an inferior CD8 T cell response compared to low-heterogeneity tumors[15].
74 Building on this, we set out to ask not only how tumor heterogeneity impacts the immune
75 response in the tumor as a whole, but also to interrogate its impact on the spatial organization
76 of the intratumoral immune response.

77 Our studies employed tumor cell lines derived from carcinogen-induced squamous cell
78 skin carcinomas, induced by dimethylbenzanthracene and 12-O-tetradecanoylphorbol-13-
79 acetate (DMBA/TPA)[17,18]. The DMBA/TPA skin carcinogenesis model gives rise to tumors that
80 exhibit a physiologically relevant range of mutational burdens[19,20] and develop in immune-
81 competent hosts, resulting in tumors with neoantigen and immune profiles that mimic those
82 found in human tumors. We have generated cell lines from DMBA/TPA-induced tumors, which,
83 when implanted into mice, give rise to tumors with reproducible immune phenotypes. Here, we
84 develop a novel model of heterogeneous tumors by implanting a mixture of two such cell lines.
85 Each cell line, labeled with a fluorophore, represents a distinct, trackable population within the
86 tumor. The two cell lines we selected share a common oncogenic driver, *Hras* Q61L, but also

87 each contain over 100 distinct nonsynonymous mutations; their combination thus models a
88 genetically heterogeneous tumor.
89 Using this novel model system, we here interrogate the mechanisms by which
90 heterogeneity in tumor cells impacts the immune response, the spatial organization of
91 infiltrating immune cells, and the response to ICB therapy. We find, not surprisingly, that the
92 "cold" tumor population drives an overall "cold" immune phenotype at a whole tumor level.
93 Further, we observe that our constituent tumor populations form a patchwork pattern within
94 the tumor. Our study reveals that the spatial organization of the tumor cells themselves creates
95 an architectural blueprint that dictates the spatial localization and function of infiltrating
96 immune cells. We observe T cells preferentially accumulating and exhibiting superior effector
97 function in the neighborhood of "hot" tumor cells, while "cold" tumor cells recruit an
98 immunosuppressive microenvironment to their immediate vicinity. The presence of the "cold"
99 tumor cells further mediates resistance to ICB therapy in mixed-population tumors. However,
100 to our surprise, we observe that immunotherapy improves the quality of the immune response
101 in "cold" tumor regions as well as "hot" regions—but not to a sufficient degree to induce robust
102 tumor regression. Our model system of heterogeneity thus illuminates how heterogeneity in
103 tumor cells impacts both the endogenous anti-tumor immune response and the efficacy of
104 therapy on a highly localized spatial scale.
105
106 **Results:**
107
108 **Modeling heterogeneous tumors with trackable tumor populations.**

109 We have established a series of squamous cell skin carcinoma cell lines, named the CIT
110 ("carcinogen-induced tumor") lines, derived from DMBA/TPA-induced skin carcinomas that
111 were initiated in *K5-CreER^{T2}-Confetti* mice on an FVB background[18]. To establish a model system
112 in which to study the impact of tumor heterogeneity on the immune response, we selected and
113 combined two of these cell lines, CIT6 and CIT9, that give rise respectively to tumors exhibiting
114 a high and low frequency of overall CD3 T cells, CD4 T cells and CD8 T cells, representing
115 immunologically "hot" and "cold" tumors. We introduced fluorescent labels into these tumor
116 cells, taking advantage of CIT lines originating from mice carrying an unactivated *Confetti*
117 cassette. We treated CIT6 and CIT9 with adenoviral Cre recombinase (AdCre), leading to
118 recombination of the Confetti allele and stochastic labeling of each cell with one of four
119 fluorescent proteins—yellow, red, cyan and green fluorescent protein (YFP, RFP, CFP and GFP,
120 respectively)[21]. We then sorted YFP$^+$ cells from the CIT6 line and RFP$^+$ cells from the CIT9 line to
121 establish fluorescently-tagged CIT6-YFP and CIT9-RFP cell lines. For all subsequent experiments,
122 these fluorescently labeled cell lines were implanted into syngeneic *Confetti* mice, carrying an
123 unactivated *Confetti* allele, which recapitulated the expected "hot" and "cold" immune
124 phenotypes (**Fig. 1A-D**; Supp Fig. 1) we observed when unlabeled CIT6 and CIT9 tumor cells
125 were implanted into wild-type FVB mice.
126 To model heterogeneous tumors, we injected mice subcutaneously with an equal
127 mixture of CIT6-YFP and CIT9-RFP cell lines (6.25×10^4 cells each, totaling 1.25×10^5 cells per
128 injection) (**Fig. 1E**). Tumors were assessed for composition by fluorescent stereomicroscope at
129 the time of harvest, when tumors were 1cm in longest diameter (21-28 days). We consistently
130 observed approximately 2/3 of the resulting tumors were comprised of both YFP$^+$ and RFP$^+$ cells

131 with clearly defined YFP$^+$ and RFP$^+$ regions, whereas the remaining 1/3 consisted of only RFP$^+$
132 cells in most cases, or only YFP$^+$ cells in rare cases (**Fig. 1F**, data not shown). The tumors that
133 contained both YFP$^+$ and RFP$^+$ cells, termed "mixed-population tumors" herein, were used for
134 downstream analyses. When the equal mixture of CIT6-YFP and CIT9-RFP cells was implanted
135 into immunodeficient NOD/SCID/IL-2Rɣ null (NSG) mice, which lack T, B and NK cells and innate
136 lymphoid cells (ILCs), we observed a higher penetrance of mixed-population tumors, indicating
137 that immune activity against tumor cells was likely responsible for cases where mixed tumors
138 failed to establish (Supp Fig. 2). Inspection of the mixed-population tumors by cryosectioning
139 and fluorescent imaging showed a patchwork of regions that could be classified as being
140 occupied primarily by YFP$^+$ cells, primarily by RFP$^+$ cells, or by a mixture of both populations
141 (**Fig. 1G**). The fluorescent tags in these cell lines thus successfully enabled spatial tracking and
142 quantification of each tumor population in the mixed-tumor population tumors and enabled us
143 to establish a novel model to study ITH.
144
145 **An immunosuppressive phenotype dominates the immune microenvironment of mixed-**
146 **population tumors.**
147 To determine how each constituent tumor population affects the overall immune
148 response in mixed-population tumors, we performed a comprehensive flow cytometric analysis
149 of the immune infiltrates (Supp Fig. 3) found in CIT6-YFP + CIT9-RFP mixed-population tumors
150 and compared this to infiltrates found in each CIT6-YFP and CIT9-RFP single-population tumors.
151 Mixed-population tumors have an overall "cold" immune phenotype, exhibiting CD4 and CD8 T
152 cell infiltration comparable to CIT9-RFP tumors and significantly lower than that found in CIT6-

153 YFP tumors (**Fig. 2A**). MHC-I proteins were expressed on more than 85% of CIT6-YFP and CIT9-
154 RFP tumor cells and expressed at a similar level (**Fig. 2B**), suggesting that the differences in T
155 cell abundance are not due to the differences in MHC-I expression. MHC-II expression was very
156 low on both CIT6-YFP and CIT9-RFP tumor cells (Supp. Fig. 4A), in line with these tumors being
157 of epithelial origin. Although there was no significant difference in the fraction of CD4 T cells
158 that were regulatory T cells (Tregs; $CD4^+$ $CD25^+$ $Foxp3^+$) or in the CD8 T cell-to-Treg ratio
159 between any of the groups, CIT9-RFP and mixed-population tumors showed a lower CD4 Teff
160 ($CD4^+$ $CD25^-$ $Foxp3^-$)-to-Treg cell ratio than CIT6-YFP tumors, suggesting a skewing in CIT9-RFP
161 and mixed tumors toward an immunosuppressive microenvironment (**Fig. 2C**). Other
162 lymphocytes, specifically B cells and $NKp46^+$ lymphocytes (including natural killer (NK) cells and
163 innate lymphoid cells (ILCs)), showed a similar pattern: CIT6-YFP tumors showed significantly
164 higher infiltration by both lymphoid populations than CIT9-RFP tumors, and mixed-population
165 tumors overall resembled CIT9-RFP tumors (although the difference between $NKp46^+$
166 lymphocytes in CIT6-YFP versus mixed tumors was not statistically significant) (**Fig. 2D**). By
167 contrast, CIT9-RFP tumors showed a higher infiltration than CIT6-YFP tumors of $F4/80^+$ $CD11b^+$
168 MHC-II^+ macrophages (**Fig. 2E**) and $CD11b^+$ myeloid cells (Supp Fig. 4B), which often harbor
169 immunosuppressive properties in the tumor microenvironment. Mixed-population tumors also
170 had an increase in $CD11b^+$ myeloid cells and a trend toward more macrophages compared to
171 CIT6-YFP tumors, again exhibiting more similarity in immune profile to CIT9-RFP tumors (**Fig. 2E,**
172 Supp Fig. 4B). $Ly6G^+$ $Ly6C^{mid}$ neutrophils, $Ly6G^-$ $Ly6C^+$ monocytes, and $CD11b^+$ $CD11c^+$ MHC-II^+
173 $F4/80^-$ dendritic cells (DCs), which are conventionally anti-tumoral effector cells, all showed a
174 trend toward lower frequency in both CIT9-RFP and mixed tumors compared to CIT6-YFP

175 tumors, albeit not statistically significant differences (Supp Fig. 4C). Collectively, these data
176 support our designation of CIT6-YFP tumors as pro-inflammatory and "immune hot," and of
177 CIT9-RFP tumors as immunosuppressive and "immune cold," and further reveal that the
178 immunosuppressive phenotype is dominant in mixed-population tumors.

179 Macrophages are conventionally known to facilitate antigen presentation and assist in T
180 cell activation, but in the context of a tumor, evidence suggests that tumor-associated
181 macrophages (TAMs) are more frequently a mediator of immunosuppression. TAMs are the
182 most abundant immune cells in CIT6-YFP and CIT9-RFP tumors, comprising 30-80% of total
183 $CD45^+$ immune cells. Therefore, we sought to determine if $F4/80^+$ $CD11b^+$ $MHC\text{-}II^+$ macrophages
184 in our tumors are functionally immunosuppressive. Macrophages were sorted from CIT6-YFP,
185 CIT9-RFP, and mixed-population tumors, and assessed for their capacity to suppress CD8 T cells
186 isolated from naïve, non-tumor bearing syngeneic *Confetti* mice and activated by CD3/CD28
187 beads. In comparison to CD8 T cells alone, the addition of TAMs significantly suppressed CD8 T
188 cell proliferation, measured as the number of cells that had undergone division (as marked by
189 CFSE dilution) (**Fig. 2F**). The expansion of activated T cells, measured as $CD69^+$ $CD25^+$ $CD8^+$ T
190 cells (early activation), $CD69^-$ $CD25^+$ $CD8^+$ T cells (late activation), or $PD\text{-}1^+$ $CD8^+$ T cells, showed
191 similar results, with the addition of macrophages decreasing the number of activated T cells
192 (**Fig. 2G**, Supp Fig. 4D). Moreover, the expansion of the $CD62L^-$ $CD44^+$ effector T cell subset and
193 the $CD62L^+$ $CD44^+$ central memory T cell subset was significantly suppressed in the presence of
194 TAMs (**Fig. 2H**, Supp Fig. 4E). Surprisingly, no difference in immunosuppressive capacity was
195 observed between TAMs derived from CIT6-YFP, CIT9-RFP or mixed-population tumors (**Fig. 2F-**
196 **H**). Thus, macrophages in CIT6-YFP, CIT9-RFP and mixed-population tumors are equally

197 immunosuppressive, but we conclude that the increased abundance of these macrophages in
198 CIT9-RFP and mixed-population tumors **(Fig. 2E)** may be responsible for creating a more
199 suppressive immune microenvironment in those tumors.
200
201 **Spatial organization of tumor populations drives the spatial organization of immune cells.**
202 Since the mixed-population tumors were comprised of a patchwork of YFP, mixed, and
203 RFP tumor regions, we next sought to better understand whether the "dominant cold" immune
204 phenotype was uniformly true in all tumor regions. To this end, we first quantified $CD3^+$ T cells
205 by immunofluorescent (IF) staining of 8µm sections. We classified each field of view as
206 predominantly occupied by CIT6-YFP cells ("YFP regions"; >60% of tumor cells are YFP^+),
207 predominantly occupied by CIT9-RFP cells ("RFP regions"; >60% of tumor cells are RFP^+), or
208 mixed ("mixed regions"; YFP and RFP each represent more than 40% of tumor cells), and then
209 quantified the number of $CD3^+$ T cells in the field (**Fig. 3A**). This analysis revealed a significantly
210 higher average count of $CD3^+$ T cells in YFP regions compared to RFP regions, with mixed
211 regions showing an intermediate level (**Fig. 3B**). Further, we observed a significant positive
212 correlation between the number of T cells and the fraction of YFP tumor cells (R^2=0.22, p=4.7 x
213 10^{-35}) in each field, and noticed that the fields of view with the highest number of infiltrating T
214 cells were all comprised of >50% YFP^+ cells (**Fig. 3C**). These data suggest that T cells
215 preferentially localize to the regions occupied by CIT6-YFP tumor cells in mixed-population
216 tumors.
217 We next turned to flow cytometry-based analysis of the immune cells in each YFP,
218 mixed, and RFP regions to gain a higher dimensional profile of the immune response in each

219 region. Mixed population tumors were embedded into agarose gel and each tumor was sliced
220 into five to ten 400µm-thick live sections. Each section was manually microdissected into YFP,
221 mixed, and RFP regions using a surgical scalpel under a fluorescent dissecting microscope. All
222 YFP pieces, all mixed pieces, and all RFP pieces from the same tumor were pooled and digested
223 into a single cell suspension for immune profiling by flow cytometry (**Fig. 3D**). Mirroring our
224 findings by IF, we found a higher frequency of total $CD3^+$ T cells in YFP regions than in RFP
225 regions, with mixed regions showing intermediate infiltration **(Fig. 3E)**. This localization pattern
226 was also seen in, and was driven by, CD4 T cells. The abundance of total T cells and CD4 T cells
227 in YFP regions of mixed-population tumors was comparable to that in single-population CIT6-
228 YFP tumors, and similarly, the abundance of total and CD4 T cells in RFP regions of mixed
229 tumors was comparable to that in single-population CIT9-RFP tumors (**Fig. 3F**). By contrast, CD8
230 T cells were at low abundance in all tumor regions, including YFP regions, and were found at
231 levels resembling those in single-population CIT9-RFP tumors (**Fig. 3G**). A more detailed analysis
232 of T cell function showed that nearly one-third of the CD4 T cells in YFP regions were Th1 cells
233 ($CD4^+$ $IFN\gamma^+$), whereas only ~2% of CD4 T cells in RFP regions were Th1 cells (median frequency
234 of Th1 cells in YFP regions = 28.9%, RFP regions = 1.99%) (**Fig. 3H**). Th2 ($CD4^+$ $IL\text{-}4^+$) and Th17
235 ($CD4^+$ $IL\text{-}17^+$) cells were equally rare in all regions (**Fig. 3I**). Even more strikingly, despite their
236 low abundance, CD8 T cells showed increased effector function in YFP regions: over 70% of CD8
237 T cells in YFP regions showed capacity to produce IFNγ, whereas less than 10% of CD8 T cells in
238 mixed and RFP regions showed the same (**Fig. 3J**). There was no apparent difference in Treg
239 ($Foxp3^+$ $CD25^+$) cell frequency between regions, but the ratio of Treg:Th1 cells and Treg: $IFN\gamma^+$
240 CD8 T cells was higher in RFP regions compared to YFP and mixed regions, suggestive of an

241 overall more immunosuppressive microenvironment in RFP regions (**Fig. 3J, K**). In addition,
242 macrophages (F4/80^{+} CD11b^{+} MHC-II^{+}) were significantly enriched in mixed regions compared
243 to YFP regions, and also trended toward higher enrichment in RFP regions (**Fig. 3L**).
244 Collectively, these data show that local tumor cells themselves play a significant role in
245 driving the immune microenvironment in their vicinity. Moreover, the observation that mixed
246 regions look similar to RFP regions—in terms of effector T cell infiltration and macrophage
247 infiltration—suggests that in regions in which both CIT6-YFP and CIT9-RFP tumor cells co-exist,
248 "cold" CIT9-RFP tumor cells exert dominance over the local immune infiltrate. The "dominant
249 coldness" of CIT9-RFP is also seen in the global suppression of CD8 T cell infiltration in all
250 regions. However, CD8 T cells that managed to infiltrate YFP regions appeared to be highly
251 active.
252
253 **CD206^{Hi} macrophages and lack of neutrophils and monocytes mediate an immunosuppressive**
254 **TME in RFP regions.**

255 To characterize immune cell spatial patterning more deeply, we employed ZipSeq spatial
256 transcriptomics[22] to CIT6-YFP + CIT9-RFP mixed-population tumors. ZipSeq allows immune cells
257 within user-defined regions of interest in live tissue sections to be tagged with distinct
258 nucleotide sequences (akin to assigning each region of interest a unique zip code), making use
259 of photocaged oligonucleotides and precise light exposure. Using this method, immune cells
260 from YFP, RFP and mixed regions of mixed population tumors (n=2) were tagged with distinct
261 "zip code" barcodes, and sections were subsequently disaggregated and subjected to single cell
262 RNA sequencing (scRNA-seq) (**Fig. 4A**). Immune cells were subjected to UMAP clustering, and

263 cluster identities were assigned based on expression of well-established markers (**Fig. 4B**, Supp
264 Fig. 5A, B). Using ZipSeq barcodes, we mapped each immune cell back to the region it
265 originated from. In line with our flow cytometry analyses, we observed a higher infiltration of T
266 cells in YFP regions compared to RFP regions (**Fig. 4C, D**), and also saw that myeloid cells
267 comprised a majority of the immune cells (**Fig. 4B**). In particular, we observed three large
268 macrophage clusters, CD206^{Hi} macrophages, MHC-II^{Hi} macrophages, and Arg1^{Hi} macrophages
269 (**Fig. 4B,** Supp Table 1). These three clusters were all enriched in RFP regions (**Fig. 4E**). By
270 contrast, neutrophils and monocytes were observed at lower abundance in RFP regions than
271 YFP regions (**Fig. 4F, G**). We carried out ZipSeq single cell spatial transcriptomics on a second
272 mixed-population tumor, and found similar results (Supp Fig. 6). Myeloid cells comprised a
273 majority of the immune cells (Supp Fig. 6A-C) and T cells were enriched in YFP regions (Supp Fig.
274 6D, E). Notably, out of seven macrophage clusters in the second tumor, six of them were
275 enriched in RFP regions compared to YFP regions (Supp Fig. 6F). Moreover, the second tumor
276 showed enrichment of neutrophils and monocytes in YFP regions (Supp Fig. 6G, H). Pathway
277 analysis with EnrichR, using genes enriched in each cluster and the GO Biological Process 2021
278 repository, suggested neutrophils had pro-inflammatory properties, as seen by neutrophil
279 activation-related genes (**Fig. 4F**, Supp Fig. 6G). Monocytes also exhibited evidence of
280 activation, with a particularly clear pro-inflammatory signature in the second tumor (**Fig. 4G**,
281 Supp Fig. 6H). Together, the combination of an enrichment of immunosuppressive
282 macrophages and a de-enrichment of inflammatory monocytes and neutrophils point to a
283 myeloid cell-driven immunosuppressive TME in RFP regions.
284

285 **Chemokine CX3CL1 is a mediator of the CIT9-RFP-driven immunosuppressive TME.**

286 To identify the drivers behind the striking spatial organization of myeloid cell infiltrates
287 in our mixed tumors, we next assessed the protein expression of a total of 44 cytokines and
288 chemokines using the lysates from CIT6-YFP and CIT9-RFP tumors. Cytokines and chemokines
289 are major mediators of immune cell localization and function, thus we hypothesized differences
290 in their expression between CIT6-YFP and CIT9-RFP might explain the differences we saw in
291 myeloid infiltrate. We found the chemokine CX3CL1 was significantly enriched in CIT9-RFP
292 tumors compared to CIT6-YFP tumors (**Fig. 5A**, Supp Fig. 7A). CX3CL1 is a chemokine with
293 reported pro-tumor properties, capable of directly promoting tumor cell proliferation and
294 migration as well as of attracting various immune cell types. To test the hypothesis that Cx3cl1
295 plays a role in driving the immunosuppressive microenvironment in our squamous cell
296 carcinomas, we generated a CIT6-YFP cell line overexpressing *Cx3cl1* and analyzed the immune
297 profile of these tumors. The abundance of macrophages was increased in Cx3cl1-
298 overexpressing tumors compared to control tumors (**Fig. 5B**). We next asked if it was a
299 particular macrophage subset(s) that showed increased abundance, and for this analysis
300 divided macrophages into the 3 main clusters we identified in our ZipSeq analysis: CD206^{Hi}
301 macrophages (CD206^{Hi} MHC-II^{Low}), MHC-II^{Hi} macrophages (CD206^{Mid} MHC-II^{Hi} Arg1^{-}) and Arg1^{Hi}
302 macrophages (CD206^{Mid} MHC-II^{Hi} Arg1^{+}) (Supp Fig. 7B). We found that CD206^{Hi} macrophages
303 were increased in frequency in Cx3cl1-overexpressing CIT6-YFP tumors compared to control
304 tumors, while the other two macrophage subsets showed no difference in frequency (**Fig. 5C**).
305 In line with this, expression of CX3CR1, a cognate receptor of CX3CL1, was the highest on
306 macrophages among all immune cell types (Supp Fig. 7C), and highest on CD206^{Hi} macrophages

307 among the three macrophage subsets (**Fig. 5D**). Additionally, we observed a lower abundance
308 of neutrophils (Ly6G^{+}) and monocytes (Ly6C^{+}) in Cx3cl1-overexpressing CIT6-YFP tumors (**Fig.**
309 **5E**). Other immune cell types including B cells, CD8 T cells and DCs showed no difference in
310 frequency (Supp Fig. 7D).

311 We next asked whether CD206^{Hi} macrophages, as the main macrophage subtype
312 increased by Cx3cl1 overexpression, had a greater capacity to suppress T cells than non-CD206^{Hi}
313 macrophages (which include both MHC-II^{Hi} and Arg1^{Hi} macrophages). We isolated CD206^{Hi} and
314 non-CD206^{Hi} macrophages from CIT9-RFP and CIT6-YFP tumors by flow cytometry-based sorting
315 (Supp Fig. 7B) and tested for their ability to suppress CD8 T cell proliferation using an *in vitro* co-
316 culture assay. We found that CD206^{Hi} macrophages could suppress T cell proliferation and
317 activation even at a low macrophage-to-CD8 T cell ratio (1:16), whereas non-CD206^{Hi}
318 macrophages could suppress CD8 T cells only at a higher co-culture ratio (1:4) (**Fig. 5F**, Supp Fig.
319 7E). Thus, while both CD206^{Hi} and non-CD206^{Hi} macrophages exhibited suppressive capacity to
320 some extent, the CD206^{Hi} macrophage subset in our tumors has a particularly strong ability to
321 suppress T cell proliferation.

322 Because we also observed an enrichment of CD206^{Hi} macrophages and lower
323 abundance of neutrophils and monocytes in RFP regions of mixed-population tumors in our
324 ZipSeq data (**Fig. 4**), we hypothesized that the CX3CL1-CX3CR1 axis plays a role in driving the
325 immunosuppressive microenvironment in these regions. There were few reads of *Cx3cl1* in the
326 ZipSeq data (data not shown) likely due to limitations associated with single cell RNAseq.
327 Therefore, to test this hypothesis, we assessed the correlation between the *Cx3cr1* expression
328 level in immune cells and their abundance in RFP regions. *Cx3cr1* transcript level was high in

329 clusters that were enriched in RFP regions (**Fig. 5G** and **Fig. 4C**; Supp Fig. 8A and Supp Fig. 6D),
330 and was the highest on the CD206^{Hi} macrophage cluster (**Fig. 5H**, Supp Fig. 8B). Moreover,
331 there was a positive correlation across clusters between the abundance of a cluster and its
332 average *Cx3cr1* transcript expression level in RFP regions, but not in YFP or mixed regions (**Fig.**
333 **5I**). Collectively, these data indicate that Cx3cl1 plays a role in driving local myeloid cell
334 abundance and enriching immunosuppressive CD206^{Hi} macrophages in RFP regions of mixed-
335 population tumors.
336
337 **An immunosuppressive tumor population drives resistance of mixed-population tumors to**
338 **anti-PD-1 blocking and CD40 agonistic antibody combination treatment.**
339 Having shown that CIT9-RFP tumor cells in mixed-population heterogeneous tumors
340 exert a dominant immunosuppressive effect and drive spatial organization within the tumor,
341 we next sought to determine if the presence of CIT9-RFP tumor cells impacts the response of
342 mixed-population tumors to immune checkpoint blockade (ICB) therapy. In particular, as an
343 immunosuppressive tumor microenvironment is linked to resistance to ICB therapy, we asked if
344 CIT9-RFP tumor cells make otherwise therapy-sensitive CIT6-YFP tumor cells resistant. We
345 tested multiple ICB combinations on our tumors, and we selected a regimen combining PD-1
346 blockade and CD40 agonist antibodies, a combination that is currently in clinical trials for
347 multiple tumor types. The combination treatment was administered in two doses at a 3-day
348 interval when the CIT6 and CIT9 tumors reached 5mm in diameter (**Fig. 6A**) and induced 50% of
349 CIT6-YFP tumors (5 out of 10 tumors) to regress completely, with 2 tumors eventually growing
350 back after 5-17 days (**Fig. 6B**). In contrast, only 9% (1 out of 11) of CIT9-RFP tumors showed a

351 decrease in tumor volume after therapy, and none achieved a complete regression (**Fig. 6B**).
352 Furthermore, the increase in the average volume of CIT6-YFP tumors over time was blunted by
353 the combination treatment in comparison to isotype control treatment, whereas CIT9-RFP
354 tumors showed similar growth kinetics in both combination treatment and isotype control arms
355 (**Fig. 6B**). This coincided with prolonged overall survival of the mice harboring CIT6-YFP tumors,
356 but not CIT9-RFP tumors, after treatment with the combination therapy (**Fig. 6C**). Thus, the
357 combination of anti-PD-1 blocking and CD40 agonistic antibodies mimics prototypical patient
358 outcomes to immunotherapy where "immune hot" tumors respond and "immune cold" tumors
359 do not. Further, this combination showed the clearest dichotomy in responses between "hot"
360 and "cold" tumors among the regimens tested, and so we chose to proceed with using it to
361 investigate how mixed-population tumors would respond.
362 We then assessed the response of tumors derived from a 1:1 mixture of CIT6-YFP and
363 CIT9-RFP cell lines to the anti-PD-1 blocking and CD40 agonistic combination treatment. The
364 combination therapy achieved complete regression (CR) in 1 out of 23 mice (4.3%) but the
365 tumor quickly grew back (**Fig. 6D**). The CR rate of mixture-derived tumors was higher than CIT9-
366 RFP single-population tumors (0% CR), but lower than CIT6-YFP tumors (50% CR) (**Fig. 6B, D**).
367 The average tumor volume was slightly smaller in the combination treatment group (**Fig. 6D**),
368 although this did not correlate to an extension of overall survival (**Fig. 6D**), suggesting therapy
369 had only a modest effect in these mixed tumors.
370 Immune profile analysis of tumors at the time of harvest (10mm in diameter) revealed
371 that CD4 and CD8 T cell infiltration was increased in both CIT6-YFP tumors and mixed tumors
372 treated with the anti-PD-1 + anti-CD40 agonist combination, and that this influx was of similar

373 magnitude in both (**Fig. 6E**). By contrast, CIT9-RFP tumors did not show a change in T cell
374 infiltration after treatment (**Fig. 6E**). However, despite the influx of T cells into mixed tumors,
375 this influx did not correspond to the same level of treatment efficacy seen in CIT6-YFP tumors.
376 Collectively, these data suggest that the presence of CIT9-RFP tumor cells dampens the
377 response of mixed tumors to the combination treatment, and also reveals an improved influx of
378 T cells into the tumor after treatment is not necessarily a marker of a successful response in the
379 context of a heterogeneous tumor.
380
381 **Spatial immune infiltration patterns persist in mixed-population tumors following anti-PD-1**
382 **blockade and CD40 agonist combination treatment.**
383 Given our previous data showing that RFP regions (and to a lesser extent, mixed regions)
384 of mixed-population tumors were spatially organized pockets of immune "coldness", we sought
385 to test the hypothesis that the immunotherapy combination treatment was acting successfully
386 in YFP regions, but failing to improve the immune response in RFP regions, leading to overall
387 failure. We applied our live tumor slice microdissection technique (**Fig. 3D**) to mixed-population
388 tumors treated with either anti-PD-1 blockade + CD40 agonist or control antibodies. The
389 immune infiltration profiles of YFP, RFP and mixed regions were analyzed 6 days after the initial
390 treatment dose, at which point tumors have not started to shrink yet (**Fig. 6B and D**). We
391 focused our analysis on T cells, as we had observed that T cell infiltration was increased by the
392 combination treatment in mixed population tumors (**Fig. 6**).
393 At the 6-day timepoint, the frequencies of overall CD4 and CD8 T cells did not differ
394 between the isotype control arm and the combination treatment arm in any of the three

395 regions (Supp Fig. 9). However, the presence of Th1 cells was dramatically increased in RFP and
396 mixed regions by the combination treatment compared to isotype control treatment (**Fig. 7A**).
397 There was also a trend toward increased Th1 cells in YFP regions, but it did not reach statistical
398 significance. The treatment-induced change in abundance was unique to Th1 cells, as other CD4
399 T cell subsets including Treg, Th2 and Th17 cells showed a similar frequency between isotype
400 control and combination treatment arms (**Fig. 7B, C**). The changes in Th1 cell abundance
401 resulted in a favorable increase in the Th1:Treg ratio in mixed and RFP regions of the
402 combination therapy-treated tumors (**Fig. 7D**). The functional impact on the CD8 T cell
403 compartment was directionally the same, but much less dramatic. The frequency of IFNγ^+ CD8 T
404 cells was modestly increased by the combination therapy in RFP regions, but not in mixed
405 regions (**Fig. 7E)**, and the IFNγ^+ CD8 T cell to Treg ratio showed a trend of improvement in mixed
406 and RFP regions in response to the treatment (**Fig. 7F**). However, because the abundance of
407 CD8 T cells remained low in all regions (as previously observed in mixed-populations tumors,
408 Fig. 3G), these improvements in CD8 T function were of small magnitude on an absolute scale.
409 Collectively, these data show that anti-PD-1 and CD40 agonist antibody treatment was
410 successful at improving the quality of the immune response in “cold” RFP and mixed tumor
411 regions—contrary to our expectations that we would only observe such improvements in the
412 “hot” YFP regions. However, despite the therapy-induced boost, the quality of the immune
413 response in RFP regions remained inferior to that in YFP regions, and the absolute number of
414 tumor-infiltrating CD8 T cells remained low. Thus, while the therapy-induced improvement in
415 anti-tumor Th1 CD4 T cell response in RFP and mixed regions likely contributed to the blunted

416 growth of treated tumors—which was also seen in this 6-day cohort (**Fig. 7G**)—it was largely
417 insufficient to mediate tumor rejection.
418
419 **Discussion**
420 Combining fluorescently tagged pro-inflammatory and immunosuppressive squamous
421 cell skin carcinoma tumor populations, we have developed a novel model system to interrogate
422 the spatial heterogeneity of tumor cells and intratumoral immune cells. When combined in a
423 1:1 ratio, we see that an immunosuppressive tumor population has a "dominant negative"
424 suppressive effect, in line with a previous report in a model of pancreatic cancer[14]. The overall
425 immune phenotype of mixed-population tumors most closely resembles that of "cold"
426 immunosuppressive tumors, and exhibits a poor infiltration of CD8 T cells—which are critical to
427 anti-tumor immunity—in all regions. Moreover, the dominant effect of the immunosuppressive
428 tumor population is also seen locally in "mixed" regions where the two tumor populations co-
429 exist.
430 However, when we look at regions locally dominated by pro-inflammatory tumor cells
431 (YFP^+ regions in our tumors), we find CD4 T cells accumulate specifically in these regions, as do
432 inflammatory monocytes and neutrophils. Both CD4 and CD8 T cells also show better effector
433 phenotypes in the vicinity of these "hot" tumor cells. By contrast, immunosuppressive
434 macrophages preferentially accumulated in the neighborhoods of "cold" tumor cells. Tumor
435 cells themselves thus set up a blueprint for the spatial architecture of infiltrating immune cells,
436 with different tumor cell populations driving distinct "micro-microenvironments" in their
437 vicinities. Our study is the first, to our knowledge, to demonstrate a clear, reproducible link

438 between spatial organization of infiltrating immune cells and the underlying spatial organization
439 of tumor cells.

440 Tumor cell-driven spatial differences in the intratumoral immune response exist at
441 baseline in the absence of therapy, but also persist during immunotherapy and exert an
442 influence on the response to therapy. Regional analysis of response to anti-PD-1 blockade +
443 anti-CD40 agonist combination immunotherapy showed a more nuanced pattern than we
444 expected: Rather than seeing a simplistic "good" response in "hot" regions and "poor" response
445 in "cold" regions, the relative influx of Th1 cells and IFNγ^+ CD8 T cells was strongest in RFP$^+$
446 "cold" regions. Nonetheless, "cold" regions remained more poorly infiltrated than "hot" regions
447 at an absolute level, even after the therapy-induced boost, indicating that therapy did not
448 entirely overcome the spatial patterning that existed pre-treatment. While the anti-PD-1 plus
449 CD40 agonist combination we employed failed to cure our mixed tumors, our model system
450 facilitated detailed region-by-region analysis of the effects and efficacy of therapy. This system
451 thus establishes a platform on which additional drug combinations or dose regimens can be
452 probed to iterate on how best to induce a productive tumor-wide anti-tumor immune response
453 across all tumor regions.

454 We identify Cx3cl1 as a mediator of a myeloid-cell-centric immunosuppressive
455 microenvironment, and a candidate driver of the "pockets of coldness" we observe in our
456 heterogeneous tumors. We show that Cx3cl1-expressing tumor cells drive enrichment of
457 immunosuppressive CD206^{Hi} macrophages, and depletion of inflammatory monocytes and
458 neutrophils. This finding is in line with previous reports of chemokine-driven spatial
459 organization of immune cells within tumors[23,24]. However, antibody depletion of Cx3cl1 was

460 insufficient to potentiate the anti-PD-1 blockade + anti-CD40 agonist combination in CIT9-RFP
461 immunosuppressive tumors (data not shown), suggesting that additional mediators of
462 immunosuppression contribute to the "coldness" of these tumors. While no single chemokine is
463 likely to potentiate a complete reversal of the immune microenvironment, identifying key
464 players that drive "pockets of coldness" is essential for better understanding how to induce a
465 robust anti-tumor response in heterogeneous tumors.

466 We have shown that local immune composition and function are both linked to the
467 identity of local tumor cells. Previous studies have suggested links between tumor genetics and
468 the anti-tumor immune response[25,26], providing a mechanistic basis by which differences in
469 local genetic mutations could drive differential patterns of local immune cells. Genetic
470 differences in tumor cells can also serve as markers of tumor populations that have evolved to
471 adopt different phenotypic behaviors from their neighbors, such as differences in chemokine
472 expression, which may or may not be direct consequences of the mutations. A multi-region
473 study of lung tumors found that "cold" regions of the tumor were more likely to be highly
474 clonally related, suggesting that some tumors had evolved a "cold" subclone—although there
475 was not a mutation reported in these clones that was promoting immune coldness directly[11].
476 Future work is expected to uncover additional pathways by which tumor cells shape their local
477 micro-microenvironments, as well as deeper insights into how immunotherapy acts on a highly
478 local spatial scale in heterogeneous tumors.

479

480 **Figure legends:**

481 **Figure 1. Modeling intratumoral heterogeneity using fluorescently-labeled DMBA/TPA-**

482 **induced squamous cell skin carcinoma cell lines.**

483 **(A-C)** Flow cytometric analysis of T cell infiltration in subcutaneous tumors derived from

484 injection of CIT6-YFP and CIT9-RFP cell lines into mice carrying an unactivated *Confetti* cassette.

485 **(D)** Immunofluorescent staining of $CD3^+$ T cells in 8µm cryosections of subcutaneous CIT6-YFP

486 and CIT9-RFP tumors, with DAPI staining cell nuclei, and quantification of T cell count per field

487 Scale bar = 100µm. **(E)** Schematic of mixed-population tumor generation. A 1:1 mixture of CIT6-

488 YFP and CIT9-RFP cell lines subcutaneously was injected into the right hind flank of mice

489 carrying an unactivated *Confetti* cassette, and the resulting tumors were harvested for

490 downstream analyses when they reached 1cm in diameter at 21-28 days post injection. **(F, G)**

491 Whole-tumor images by fluorescent dissecting microscope (F) and a representative image of a

492 tumor cross-section (8µm cryosection) (G) of tumors that were a 1:1 mixture of CIT6-YFP and

493 CIT9-RFP cell lines. Scale bars in (F) and (G) are 2mm and 1mm respectively. All data are a

494 representation of at least 3 independent experiments.

495

496 **Figure 2. The immunosuppressive tumor population drives an overall immunosuppressive**

497 **phenotype in mixed-population tumors.**

498 **(A-E)** Flow cytometric immune profiling of tumors derived from CIT6-YFP and CIT9-RFP cell lines

499 and mixed-population tumors derived from a 1:1 mixture of the two cell lines, including **(A)** T

500 cells, CD4 T cells and CD8 T cells, **(B)** frequency of tumor cells ($CD45^-$ YFP^- or $CD45^-$ RFP^-)

501 expressing MHC-I molecules (H2-K^q and H2-L^qD^q) (left) and median fluorescence intensity (MFI)

502 of the MHC-I molecules on H2-K^q and H2-L^qD^q double positive tumor cells (right), **(C)** Treg

503 (Foxp3$^+$ CD25$^+$) frequency, CD8 T cell-to-Treg ratio, and effector CD4 T cell (Teff, Foxp3$^-$ CD25$^-$)-
504 to-Treg ratio, **(D)** B cells (B220$^+$) and natural killer (NK) or innate lymphoid cell (ILC) (NKp46$^+$)
505 lymphocytes and **(E)** macrophages (F4/80$^+$ CD11b$^+$ MHC-II$^+$). Data in (A)-(E) are a representation
506 of at least two independent experiments with ≥5 mice per experiment. **(F-H)** *In vitro* CD8 T cell
507 suppression by macrophages sorted from the tumors. CFSE-stained and CD3/28 beads-
508 stimulated CD8 T cells isolated from naïve *Confetti* mice were co-cultured with tumor-
509 associated macrophages (TAM) at varying ratios and analyzed for proliferation via CFSE signal
510 and activation markers. Data are a representation of 2 independent experiments, with 3
511 biological replicates in each experiment. **(F)** Representative histogram showing the CFSE signal
512 in CD8 T cells, with gates marking divided cells, defined as the cells that have divided more than
513 twice (left) and graph showing the count of divided cells (right). "No TAM", T cell stimulation
514 control without macrophages; "No stim", control with no T cell stimulation. **(G)** Count of
515 activated (CD69$^+$ CD25$^+$) CD8 T cells, **(H)** Count of effector CD8 T cell subsets marked by
516 combinations of CD62L and CD44 expression.
517
518 **Figure 3. Spatial organization of tumor populations drives the spatial organization of immune**
519 **cells.**
520 **(A)** Representative cross-section images showing examples of a YFP, mixed and RFP region of a
521 mixed-population tumor and CD3 stain. **(B)** Quantification of CD3$^+$ T cells per field, plotted for
522 each region. **(C)** Correlation of YFP$^+$ cell fraction and CD3$^+$ T cell frequency in each field. CD3$^+$ T
523 cell count was scaled to DAPI$^+$ cell count in each field to normalize the difference in cell density
524 between fields. **(D)** Schematic of immune cell profiling in YFP, mixed and RFP regions of mixed-

525 population tumors. Each mixed-population tumor was sliced into five to ten 400µm-thick live
526 sections, and each section was manually microdissected into YFP, mixed, and RFP regions using
527 a surgical scalpel under a fluorescent dissecting microscope. All YFP pieces, all mixed pieces,
528 and all RFP pieces from the same tumor were pooled for immune profiling by flow cytometry.
529 White scale bar = 5mm, blue scale bar = 1mm. **(E-L)** Frequency of T cell subsets, ratio of Treg to
530 IFNγ^+ CD8 T cells or Th1 cells, and frequency of macrophages in YFP, mixed and RFP regions.
531 Grey dotted lines in panels (E), (F), (G) and (L) separate data of mixed-population tumors from
532 the data of single-population tumors. All data are a representation of two independent
533 experiments, with ≥3 mice per experiment (B,C) or ≥6 mice per experiment (E-L).
534
535 **Figure 4. CD206^{Hi} macrophages and lack of neutrophils and monocytes mediate an**
536 **immunosuppressive TME in RFP regions.**
537 **(A)** Schematic of ZipSeq spatial transcriptomic analysis of mixed-population tumors. Composite
538 stitched image of a 200µm-thick live section marked with YFP regions (encircled with green
539 lines), RFP regions (red lines) and mixed regions (blue lines) is shown. YFP, RFP and mixed
540 regions were illuminated individually to allow for the binding of a unique barcode ("zipcode") to
541 a photocaged oligo-CD45 antibody complex. ZipCode-tagged immune cells were analyzed by
542 scRNAseq. **(B)** Uniform manifold approximation and projection (UMAP) representation of
543 zipcode-labeled cells with cluster overlay. n = 3,238 cells, n_{YFP} = 1,236, n_{RFP} = 1,318, n_{Mixed} = 684.
544 **(C)** UMAP representation of zipcode-labeled cells with zipcode identity overlaid. **(D)** Abundance
545 of cells belonging to the T cell cluster (cluster 9), calculated as percentage of total immune cells
546 in each region. **(E)** Abundance of cells belonging to MHC-II^{Hi}, Arg1^{Hi} and CD206^{Hi} macrophage

547 clusters (clusters 1, 2, and 3 respectively), calculated as percentage of total immune cells in
548 each region. **(F)** Percentage of cells belonging to neutrophil cluster (cluster 7) in each region and
549 pathway analysis showing the gene families enriched in the neutrophil cluster based on the top
550 250 differentially expressed genes. **(G)** Percentage of cells belonging to monocyte cluster
551 (cluster 6) and pathway analysis of genes enriched in the monocyte cluster based on the top 31
552 differentially expressed genes.
553
554 **Figure 5. Chemokine Cx3cl1 mediates the CIT9-RFP-driven immunosuppressive TME.**
555 **(A)** ELISA-based quantification of CX3CL1 using tumor lysates of CIT6-YFP and CIT9-RFP single-
556 population tumors (n=3 per cell line) **(B, C)** Infiltration of total macrophage (B) and macrophage
557 subsets (C) in CIT6-YFP tumors overexpressing CX3CL1 (CIT6-YFP^{Cx3cl1}) and empty vector (CIT6-
558 YFP^{Empty}). **(D)** Expression of CX3CR1 on macrophage subsets in CIT6-YFP^{Cx3cl1} tumors, measured
559 as MFI from flow cytometric analysis. **(E)** Frequency of neutrophils and monocytes in CX3CL1-
560 overexpressing CIT6-YFP tumors. Data in (B)-(E) are representation or combination of two
561 independent experiments with ≥10 mice per experiment. **(F)** CD8 T cell suppression assay using
562 CD206^{Hi} macrophages and a pool of Arg1^{Hi} macrophages and MHC-II^{Hi} macrophages (Non-
563 CD206^{Hi} TAMs) isolated from CIT6-YFP and CIT9-RFP single-population tumors. Representation
564 of two independent experiments with at least 2 mice per arm. **(G)** Feature plot overlaid on
565 UMAP representation for *Cx3cr1* gene from the tumor analyzed by ZipSeq in Fig. 4. **(H)** Violin
566 plot showing *Cx3cr1* distribution based on cluster identity. **(I)** Correlation between an average
567 relative *Cx3cr1* transcript level of each cluster and the percentage of cells belonging to the
568 cluster. Combined analysis of two tumors analyzed in Fig. 4 and Supp Fig. 6.

569

570 **Figure 6. An immunosuppressive tumor population drives resistance of mixed-population**

571 **tumors to anti-PD-1 blocking and CD40 agonistic antibody combination treatment.**

572 **(A)** Dosing schedule of anti-PD-1 and CD40 agonist treatment. **(B)** Tumor growth curves of CIT6-

573 YFP and CIT9-RFP tumors showing tumor volume of individual tumors and average volume of

574 isotype control and anti-PD-1+CD40 agonist combination treatment arms. Red arrows under

575 the x axis shows the timing of treatments (day 0 and 3), fraction shown on the top right corner

576 of individual tumor volume plots shows the number of mice whose tumors completely

577 regressed post-treatment. **(C)** Kaplan-Meier curves comparing the survival of mice from each

578 treatment arm. Statistical test was performed using log-rank test. **(D)** Tumor growth and

579 survival of mice harboring tumors derived from a 1:1 mixture of CIT6-YFP and CIT9-RFP cell

580 lines. **(E)** Frequency of tumor-infiltrating T cells post-treatment in CIT6-YFP, CIT9-RFP, and 1:1

581 mixture-derived tumors. All experiments were performed with at least 8 mice per treatment

582 arm.

583

584 **Figure 7. Spatial immune infiltration patterns persist in mixed-population tumors following**

585 **anti-PD-1 blockade and CD40 agonist combination treatment.**

586 **(A–F)** Tumors derived from a 1:1 mixture of CIT6-YFP and CIT9-RFP cell lines were treated with

587 α-PD-1 +CD40 agonist combination treatment or isotype control antibodies at day 0 and 3 and

588 analyzed at day 6 for spatial T cell infiltration profile via microdissection and flow-based

589 analysis. **(A)** Th1 cell frequency in each region of isotype control-treated and combination

590 therapy-treated tumors, **(B)** Treg frequency, **(C)** Frequency of Th1, Th2, Th17 and Treg cells, **(D)**

591 Th1-to-Treg ratio, **(E)** Frequency of IFNγ^+ CD8 T cells and **(F)** IFNγ^+ CD8 T cell to Treg ratio. **(G)**
592 Average tumor volume of each treatment arm. Red arrows under the x axis shows the timing of
593 treatments. Experiment was performed with at least 10 mice per treatment/tumor arm.
594
595
596 **Materials and methods:**
597 Carcinogenesis and cell line generation
598 To induce tumors, *K5-CreER^{T2}-Confetti FVB/N* mice were treated with 25 mg DMBA followed by
599 TPA (200 µl of a 10^{-4} M solution in acetone) two times a week for 20 weeks, as described[18]. To
600 generate cell lines, carcinomas were resected at a size of >1 cm in longest diameter, finely
601 chopped, digested in DMEM containing Collagenase I and IV and DNase I for 45 minutes at
602 37 °C, washed with PBS, plated in supplemented DMEM (high-glucose DMEM (Gibco, catalog#
603 11995065) plus 10% heat-inactivated FBS (Gibco), 2mM L-glutamine, with 100 units/ml
604 penicillin, 100 µg/ml streptomycin, and 2.5 µg/ml amphotericin B (Gibco)), and passaged until
605 cells stably grow in culture. The established cell lines were cultured in the supplemented DMEM
606 for all experiments.
607
608 Cell line labeling
609 Unlabeled cell lines were treated with adenoviral Cre recombinase (Vector Biolabs catalog
610 #1045) to induce labeling with Confetti fluorescent proteins. YFP- and RFP-expressing cells were
611 sorted via fluorescence-activated cell sorter and further grown in vitro to establish CIT6-YFP and
612 CIT9-RFP cell lines.

613

614 In vivo experiments

615 A total of 1.25 x 10^5 cells were injected subcutaneously into the dorsal flank of 8 to 16 week-old
616 male and female *Confetti*-homozygous *FVB/N* mice. Approximately 21-28 days later, when
617 tumors measured ~1cm in diameter, tumors were dissected and digested as described above,
618 and subsequently used in flow cytometric analysis. For treatment experiments, when tumors
619 measured approximately 5mm in diameter, mice were injected intraperitoneally with one dose
620 (CD40 agonistic antibody) or two doses (anti-PD-1 antibody) of therapeutic antibodies,
621 administered at a three day interval. Antibodies used were rat anti-mouse PD-1 IgG2a antibody
622 (RMP1-14, BioXCell), rat anti-CD40 agonist IgG2a antibody (FGK4.5, BioXCell), and rat IgG2a
623 isotype control (2A3; BioXCell) at 200µg per antibody per dose. Tumors were resected at 1cm in
624 diameter and used for downstream analyses, except in 6-day post-treatment analyses where
625 tumors were resected 6 days after treatment initiation. All animal experiments were approved
626 by the University of California San Francisco Laboratory Animal Resource Center (IUCAC;
627 AN187679). This work complies with all the relevant ethical regulations regarding animal
628 research.

629

630 Flow cytometric immune profiling and macrophage cell sorting

631 For whole tumor analysis and sorting, 5 million cells were stained with antibodies. For spatial
632 immune profiling, tumors were embedded in 2% agarose gel, sliced into 400µm section by a
633 Leica Vibratome, microdissected into YFP, RFP and mixed regions using surgical scalpel while
634 visualizing each region on MVX10 fluorescent stereoscope. Multiple pieces of each region from

635 a single tumor were pooled for digestion, followed by flow cytometric analysis. Cell sorting was
636 performed on FACS Aria III (BD Biosciences). Antibodies used for flow cytometric analyses and
637 sorting are listed in Table 2.
638
639 Immunofluorescence imaging
640 After half of the tumors were processed for flow cytometric analysis, the remaining halves were
641 fixed in 4% paraformaldehyde for 2 hours, dehydrated in PBS with 30% sucrose overnight at
642 4C°, embedded in Tissue-tek O.C.T. compound (Sakura Finetek USA) and stored at -80C°.
643 Embedded blocks were cryosectioned into 8µm sections using Leica CM3050 S Cryostat (Leica
644 Biosystems) and stained with rabbit anti-mouse CD3 antibody (ab5690, Abcam) overnight,
645 followed by stain with secondary anti-rabbit Alexa Fluor 647 antibody (Invitrogen) for 1 hour at
646 room temperature and DAPI stain for 5 minutes. Fluorescence image was taken on microscope
647 (DMi8, Leica Biosystems) using Leica Application Suite X (Leica Biosystems) imaging software,
648 and fraction of YFP+ and RFP+ cells as well as the number of CD3+ cells in each tile were
649 quantified using CellProfiler ver. 3.1.9.
650
651 Overexpression of cytokines and chemokines
652 Mouse *Cx3cl1* gene was amplified using forward primer 5' -aactcgagatggctccctcgccgctcg -3' and
653 reverse primer 5' -ttccgcggtcacactggcaccaggacgta- 3', cDNAs generated from CIT9 cell line and
654 Q5® High-Fidelity DNA polymerase (NEB). MSCV 2.2-IRES-CFP retroviral vector was generated
655 by replacing GFP of MSCV 2.2-IRES-GFP vector (obtained from James Carlyle lab at University of
656 Toronto) with CFP. Using restriction enzymes XhoI and SacII, *Cx3cl1* coding sequencing was

657 cloned into MSCV 2.2-IRES-GFP vector. Proviral vectors Gag/Pol and VSV-G were co-transfected
658 with Cx3cl1-IRES-GFP MSCV2.2 vector using lipofectamine 3000 (Invitrogen) into HEK293T cells.
659 48 hours later, the viruses were collected, mixed with CIT6-YFP cells and spinfected at 800g for
660 90 minutes. YFP^+ CFP^+ transduced cells were sorted 72 hours post-transduction.
661
662 ZipSeq spatial transcriptomics analysis
663 Mixed-population tumors were harvested at 1cm in diameter and sliced into 200µm section in
664 2% agarose using vibratome. Section was incubated with CD45 antibody linked to Cy5-
665 conjugated photocaged oligo for 1 hour at 4C°, followed by patterned illumination of a user-
666 defined region of interest[22] and incubation with a unique ZipCode. The process was repeated
667 for YFP, RFP and mixed regions. The section then was digested in a Collagenase I and IV blend
668 for 30 minutes at room temperature, and sorted for live $Cy5^+$ cells using FACS Aria II. washed in
669 PBS + 0.04% BSA and then encapsulated following 10× Genomics specifications for 3' v3
670 chemistry with target cell number of 8,000.
671 Libraries were sequenced with a target number of 30,000 reads per cell for gene
672 expression and 3,000 reads per cell for ZipCode barcodes on a Illumina NovaSeq. Demultiplexed
673 fastqs were aligned using CellRanger to the mm10 Ensembl 93 reference genome. Count
674 matrices were used to generate Seurat objects in R keeping only cells with at least 200 detected
675 genes and genes found in at least 3 cells. Cells were further filtered based on a minimum 500
676 gene cutoff and maximum 15% mitochondrial reads. ZipCode counts were normalized using
677 centered log ratio transform and then assigned a dominant ZipCode identity (as in [22]). Cells
678 were then passed through SCTransform regressing for percent mitochondrial reads. Following

679 PCA analysis on the top variable genes, the first 18 principal components were used as inputs
680 for UMAP dimensional reduction and clustering via the FindNeighbors and FindClusters
681 commands. For pathway analysis, lists of genes with average Log_2 fold change >1 for each
682 cluster were used as input for GO Biological Process 2021 repository on EnrichR
683 (https://maayanlab.cloud/Enrichr/).
684
685 Cytokine array
686 70-150mg of tumor pieces were chopped into small pieces in RIPA buffer containing proteinase
687 inhibitor (Cell BioLabs) and homogenized using OctoMACS (Miltenyi Biotec). The homogenate
688 was centrifuged at 400g for 5 minutes followed by further centrifugation at 10,000g for 10
689 minutes at 4C°. The supernatant was collected and stored at -80C°. Protein concentration was
690 measured using DC protein assay kit (BioRad). The sample concentrations were normalized
691 prior to the submission for the analysis by Eve Technologies DM-44 mouse Discovery Assay
692 panel.
693
694 *In vitro* T cell suppression co-culture assay
695 CD8 T cells were isolated from the lymph node of naïve mice with unactivated Confetti cassette
696 using EasySep™ Mouse $CD8^+$ T Cell Isolation Kit (StemCell Technologies) and macrophages were
697 sorted from the tumors via FACS sorting. CD8 T cells were labeled with CFSE and co-cultured
698 with the macrophages at varying ratios in the presence of Mouse T-Activator CD3/CD28
699 Dynabeads™ (Gibco) and analyzed for division and T cell activation markers.
700

701 Statistical analysis

702 Data were analyzed using Prism 9 (GraphPad) with either Student's t-test for experiments with
703 two arms, one-way ANOVA analysis for experiments with one variable and more than 3
704 experiment conditions, or two-way ANOVA for experiments with two variables and more than 3
705 experiment conditions. Statistical tests for spatial analyses (Fig. 3 and 7) were done using
706 Student's t-test. For Kaplan-Meier survival analyses, log-rank test was used. Graphs show mean
707 ± SEM or mean ± SD; *, $p < 0.05$; **, $p < 0.01$; ***, $p < 0.001$.

708

709 **Acknowledgements**

710 This work was supported by the UCSF Program for Breakthrough Biomedical Research (PBBR)
711 Sandler Fellowship, US National Cancer Institute (NCI) grant R21CA264599, the Huntsman
712 Cancer Institute Cancer Center Support Grant P30CA040214, the Parker Institute for Cancer
713 Immunotherapy, the American Cancer Society, and The Cancer League. We thank the UCSF
714 Biological Imaging Development CoLab and UCSF Parnassus Flow CoLab, RRID:SCR_018206.
715 Some images were created with BioRender.com.

716

717 **Author Contributions**

718 M.T., L.L., C.L.-S., and M.Q.R. designed the project and experiments. M.T. and L.L. led all
719 experiments and data analyses. K.H. and M.T. carried out the ZipSeq single cell transcriptomics
720 experiments and analysis, with support from M.K. M.T. and M.Q.R. wrote the manuscript, with
721 input from other co-authors. K.K., D.S., K.N., and Z.A. assisted with experiments. L.F. provided
722 guidance to the studies.

723

724 **References**

725 1. Ribas, A. & Wolchok, J. D. Cancer immunotherapy using checkpoint blockade. *Science*
726 *(1979)* **1355**, 1350–1355 (2018).

727 2. Chen, D. S. & Mellman, I. Elements of cancer immunity and the cancer-immune set point.
728 *Nature* **541**, 321–330 (2017).

729 3. Das, S. & Johnson, D. B. Immune-related adverse events and anti-tumor efficacy of
730 immune checkpoint inhibitors. *Journal for ImmunoTherapy of Cancer* vol. 7 Preprint at
731 https://doi.org/10.1186/s40425-019-0805-8 (2019).

732 4. Darvin, P., Toor, S. M., Sasidharan Nair, V. & Elkord, E. Immune checkpoint inhibitors:
733 recent progress and potential biomarkers. *Experimental and Molecular Medicine* vol. 50
734 Preprint at https://doi.org/10.1038/s12276-018-0191-1 (2018).

735 5. McGranahan, N. *et al.* Clonal neoantigens elicit T cell immunoreactivity and sensitivity to
736 immune checkpoint blockade. *Science (1979)* **351**, 1463–1469 (2016).

737 6. McGranahan, N. & Swanton, C. Clonal Heterogeneity and Tumor Evolution: Past, Present,
738 and the Future. *Cell* **168**, 613–628 (2017).

739 7. Liu, D. *et al.* Integrative molecular and clinical modeling of clinical outcomes to PD1
740 blockade in patients with metastatic melanoma. *Nat Med* **25**, 1916–1927 (2019).

741 8. Gerlinger, M. *et al.* Intratumor Heterogeneity and Branched Evolution Revealed by
742 Multiregion Sequencing. *New England Journal of Medicine* **366**, 883–92 (2012).

743 9. Hu, X. *et al.* Multi-region exome sequencing reveals genomic evolution from
744 preneoplasia to lung adenocarcinoma. *Nat Commun* **10**, (2019).

745 10. Turajlic, S. *et al.* Deterministic Evolutionary Trajectories Influence Primary Tumor
746 Growth: TRACERx Renal. *Cell* **173**, 595-610.e11 (2018).
747 11. Abduljabbar, K. *et al.* Geospatial immune variability illuminates differential evolution of
748 lung adenocarcinoma. *Nat Med* https://doi.org/10.1038/s41591-020-0900-x (2020).
749 12. Nirmal, A. J. *et al.* The Spatial Landscape of Progression and Immunoediting in Primary
750 Melanoma at Single-Cell Resolution. *Cancer Discov* **12**, 1518–1541 (2022).
751 13. Mitra, A. *et al.* Spatially resolved analyses link genomic and immune diversity and reveal
752 unfavorable neutrophil activation in melanoma. *Nat Commun* **11**, 1–18 (2020).
753 14. Li, J. *et al.* Tumor Cell-Intrinsic Factors Underlie Heterogeneity of Immune Cell Infiltration
754 and Response to Immunotherapy. *Immunity* **49**, 178-193.e7 (2018).
755 15. Wolf, Y. *et al.* UVB-Induced Tumor Heterogeneity Diminishes Immune Response in
756 Melanoma. *Cell* **179**, 219-235.e21 (2019).
757 16. Gejman, R. S. *et al.* Rejection of immunogenic tumor clones is limited by clonal fraction.
758 *Elife* **7**, 1–22 (2018).
759 17. Wong, C. E. *et al.* Inflammation and Hras signaling control epithelial-mesenchymal
760 transition during skin tumor progression. *Genes Dev* **27**, 670–82 (2013).
761 18. Reeves, M. Q., Kandyba, E., Harris, S., del Rosario, R. & Balmain, A. Multicolour lineage
762 tracing reveals clonal dynamics of squamous carcinoma evolution from initiation to
763 metastasis. *Nat Cell Biol* **20**, 699–709 (2018).
764 19. McCreery, M. Q. *et al.* Evolution of metastasis revealed by mutational landscapes of
765 chemically induced skin cancers. *Nat Med* **21**, 1514–1520 (2015).

766 20. Nassar, D., Latil, M., Boeckx, B., Lambrechts, D. & Blanpain, C. Genomic landscape of
767 carcinogen-induced and genetically induced mouse skin squamous cell carcinoma. *Nat*
768 *Med* **21**, (2015).
769 21. Snippert, H. J. *et al.* Intestinal Crypt Homeostasis Results from Neutral Competition
770 between Symmetrically Dividing Lgr5 Stem Cells. *Cell* **143**, 134–144 (2010).
771 22. Hu, K. H. *et al.* ZipSeq: barcoding for real-time mapping of single cell transcriptomes. *Nat*
772 *Methods* **17**, 833–843 (2020).
773 23. Miheecheva, N. *et al.* Multiregional single-cell proteogenomic analysis of ccRCC reveals
774 cytokine drivers of intratumor spatial heterogeneity. *Cell Rep* **40**, (2022).
775 24. Pelka, K. *et al.* Spatially organized multicellular immune hubs in human colorectal cancer.
776 *Cell* **184**, 4734-4752.e20 (2021).
777 25. Wellenstein, M. D. *et al.* Loss of p53 triggers WNT-dependent systemic inflammation to
778 drive breast cancer metastasis. *Nature* (2019) doi:10.1038/s41586-019-1450-6.
779 26. Wellenstein, M. D. & de Visser, K. E. Cancer-Cell-Intrinsic Mechanisms Shaping the Tumor
780 Immune Landscape. *Immunity* **48**, 399–416 (2018).
781

Figure 1

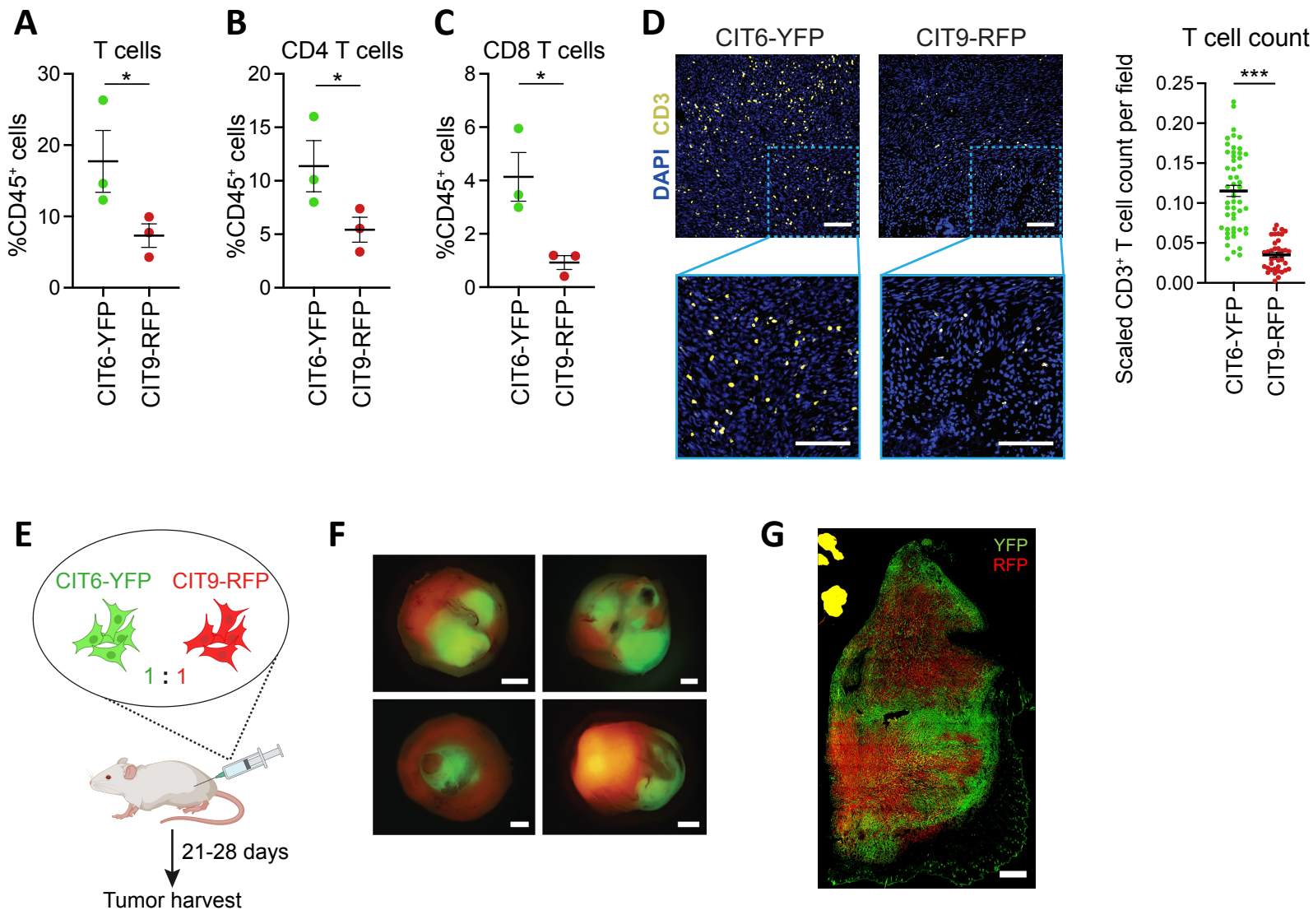
A
T cells
%CD45⁺ cells
30
20
10
0
*
CIT6-YFP
CIT9-RFP
B
CD4 T cells
%CD45⁺ cells
20
15
10
5
0
*
CIT6-YFP
CIT9-RFP
C
CD8 T cells
%CD45⁺ cells
8
6
4
2
0
*
CIT6-YFP
CIT9-RFP
D
CIT6-YFP
CIT9-RFP
DAPI CD3
T cell count
Scaled CD3⁺ T cell count per field
0.25
0.20
0.15
0.10
0.05
0.00
***
CIT6-YFP
CIT9-RFP
E
CIT6-YFP
CIT9-RFP
1 : 1
21-28 days
Tumor harvest
F
G
YFP
RFP

Figure 2

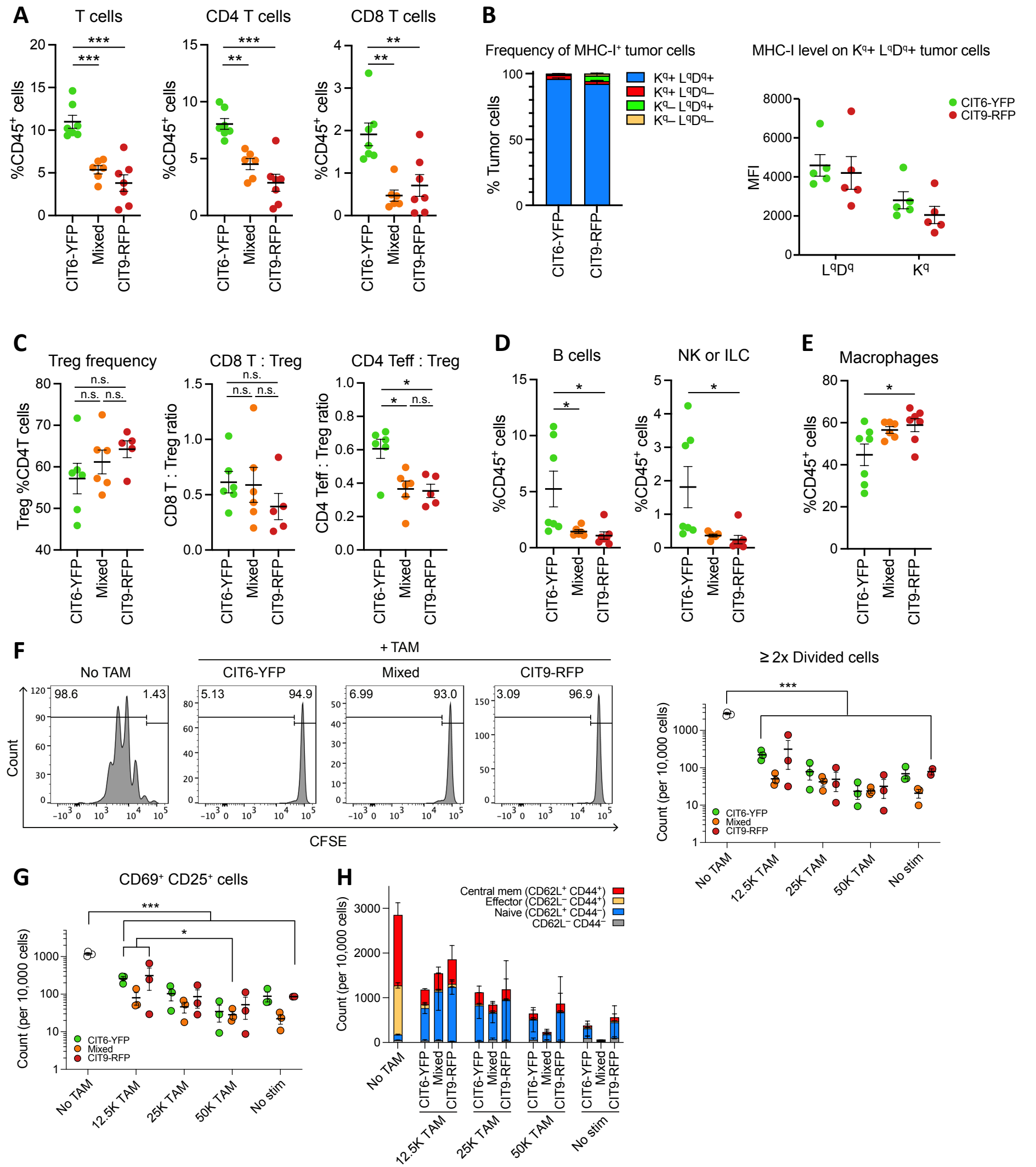
A
T cells
CD4 T cells
CD8 T cells
%CD45+ cells
CIT6-YFP
Mixed
CIT9-RFP
B
Frequency of MHC-I+ tumor cells
% Tumor cells
Kq+ LqDq+
Kq+ LqDq–
Kq– LqDq+
Kq– LqDq–
MHC-I level on Kq+ LqDq+ tumor cells
MFI
LqDq
Kq
C
Treg frequency
CD8 T : Treg
CD4 Teff : Treg
Treg %CD4T cells
CD8 T : Treg ratio
CD4 Teff : Treg ratio
n.s.
D
B cells
NK or ILC
E
Macrophages
F
+ TAM
No TAM
CIT6-YFP
Mixed
CIT9-RFP
98.6
1.43
5.13
94.9
6.99
93.0
3.09
96.9
Count
CFSE
≥ 2x Divided cells
Count (per 10,000 cells)
No TAM
12.5K TAM
25K TAM
50K TAM
No stim
G
CD69+ CD25+ cells
H
Central mem (CD62L+ CD44+)
Effector (CD62L– CD44+)
Naive (CD62L+ CD44–)
CD62L– CD44–

Figure 3

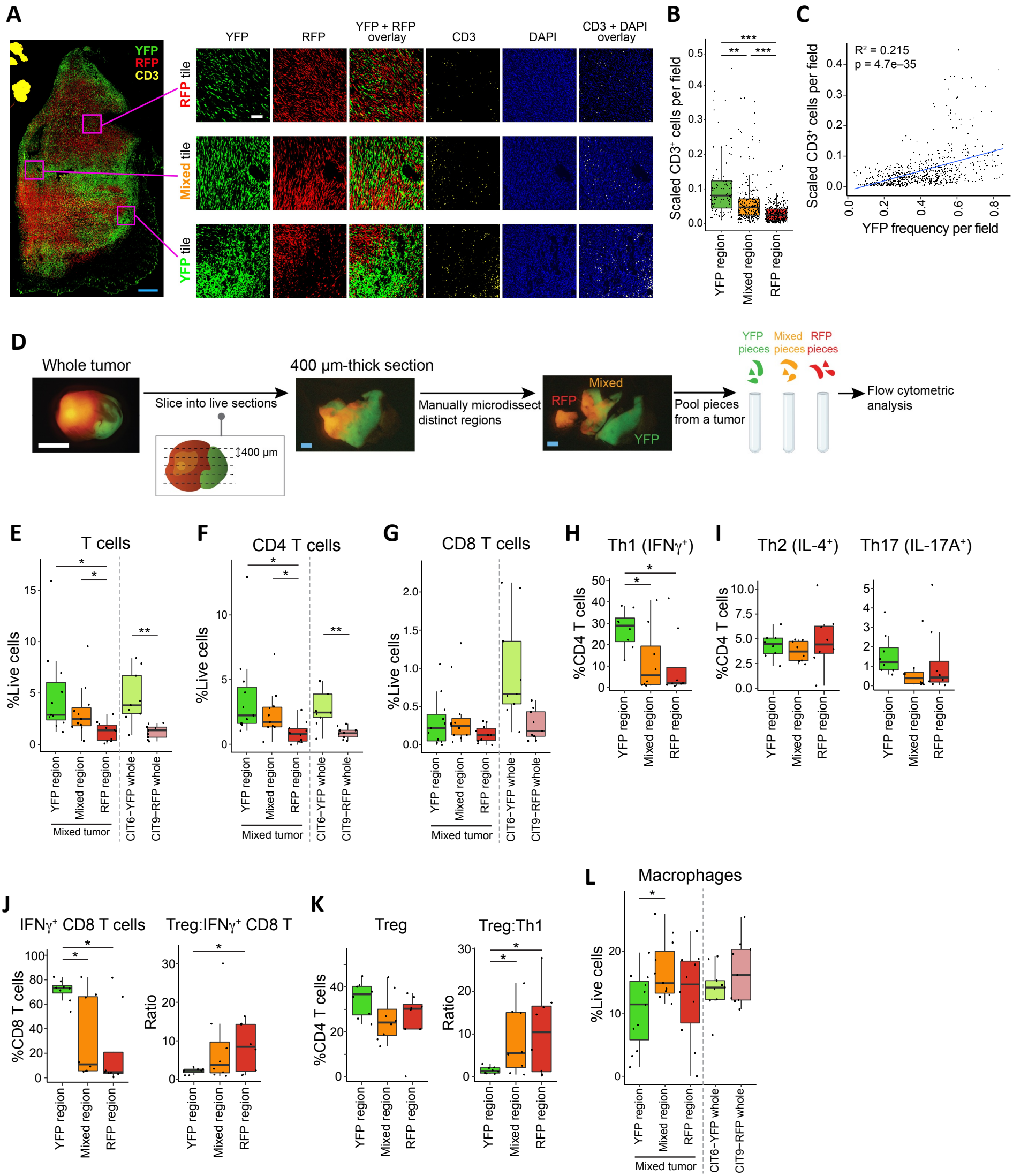
A
YFP
RFP
CD3
YFP
RFP
YFP + RFP overlay
CD3
DAPI
CD3 + DAPI overlay
RFP tile
Mixed tile
YFP tile
B
Scaled CD3⁺ cells per field
YFP region
Mixed region
RFP region
C
R² = 0.215
p = 4.7e–35
Scaled CD3⁺ cells per field
YFP frequency per field
D
Whole tumor
Slice into live sections
400 µm
400 µm-thick section
Manually microdissect distinct regions
Mixed
RFP
YFP
Pool pieces from a tumor
YFP pieces
Mixed pieces
RFP pieces
Flow cytometric analysis
E
T cells
%Live cells
Mixed tumor
CIT6–YFP whole
CIT9–RFP whole
F
CD4 T cells
G
CD8 T cells
H
Th1 (IFNγ⁺)
%CD4 T cells
I
Th2 (IL-4⁺)
Th17 (IL-17A⁺)
J
IFNγ⁺ CD8 T cells
%CD8 T cells
Treg:IFNγ⁺ CD8 T
Ratio
K
Treg
Treg:Th1
L
Macrophages

Figure 4

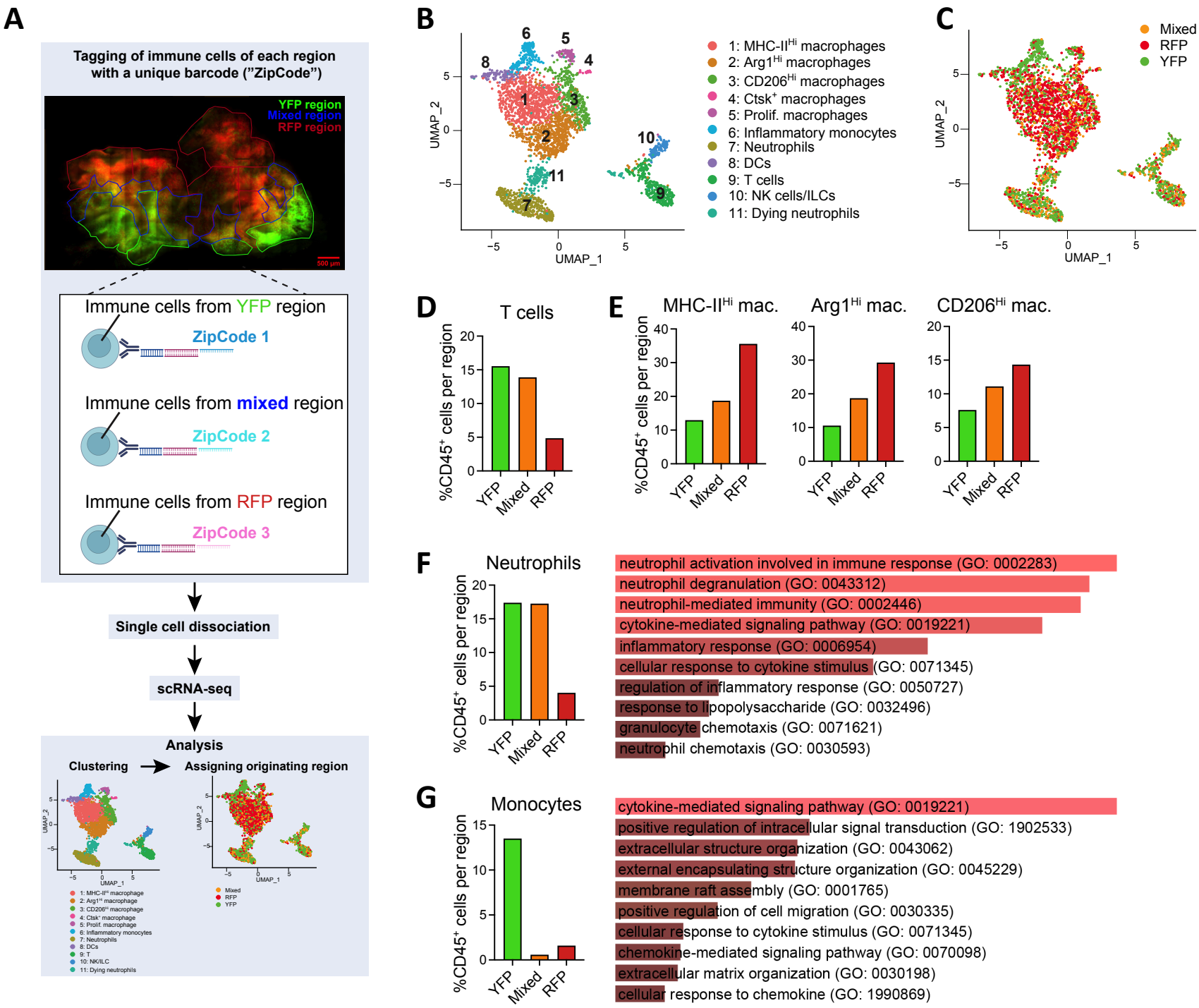
A
Tagging of immune cells of each region with a unique barcode ("ZipCode")
YFP region
Mixed region
RFP region
500 µm
Immune cells from YFP region
ZipCode 1
Immune cells from mixed region
ZipCode 2
Immune cells from RFP region
ZipCode 3
Single cell dissociation
scRNA-seq
Analysis
Clustering
Assigning originating region
UMAP_1
UMAP_2
1: MHC-II^Hi macrophage
2: Arg1^Hi macrophage
3: CD206^Hi macrophage
4: Ctsk^+ macrophage
5: Prolif. macrophage
6: Inflammatory monocytes
7: Neutrophils
8: DCs
9: T
10: NK/ILC
11: Dying neutrophils
Mixed
RFP
YFP
B
1: MHC-II^Hi macrophages
2: Arg1^Hi macrophages
3: CD206^Hi macrophages
4: Ctsk^+ macrophages
5: Prolif. macrophages
6: Inflammatory monocytes
7: Neutrophils
8: DCs
9: T cells
10: NK cells/ILCs
11: Dying neutrophils
C
Mixed
RFP
YFP
D
T cells
%CD45^+ cells per region
YFP
Mixed
RFP
E
MHC-II^Hi mac.
Arg1^Hi mac.
CD206^Hi mac.
F
Neutrophils
neutrophil activation involved in immune response (GO: 0002283)
neutrophil degranulation (GO: 0043312)
neutrophil-mediated immunity (GO: 0002446)
cytokine-mediated signaling pathway (GO: 0019221)
inflammatory response (GO: 0006954)
cellular response to cytokine stimulus (GO: 0071345)
regulation of inflammatory response (GO: 0050727)
response to lipopolysaccharide (GO: 0032496)
granulocyte chemotaxis (GO: 0071621)
neutrophil chemotaxis (GO: 0030593)
G
Monocytes
cytokine-mediated signaling pathway (GO: 0019221)
positive regulation of intracellular signal transduction (GO: 1902533)
extracellular structure organization (GO: 0043062)
external encapsulating structure organization (GO: 0045229)
membrane raft assembly (GO: 0001765)
positive regulation of cell migration (GO: 0030335)
cellular response to cytokine stimulus (GO: 0071345)
chemokine-mediated signaling pathway (GO: 0070098)
extracellular matrix organization (GO: 0030198)
cellular response to chemokine (GO: 1990869)

Figure 5

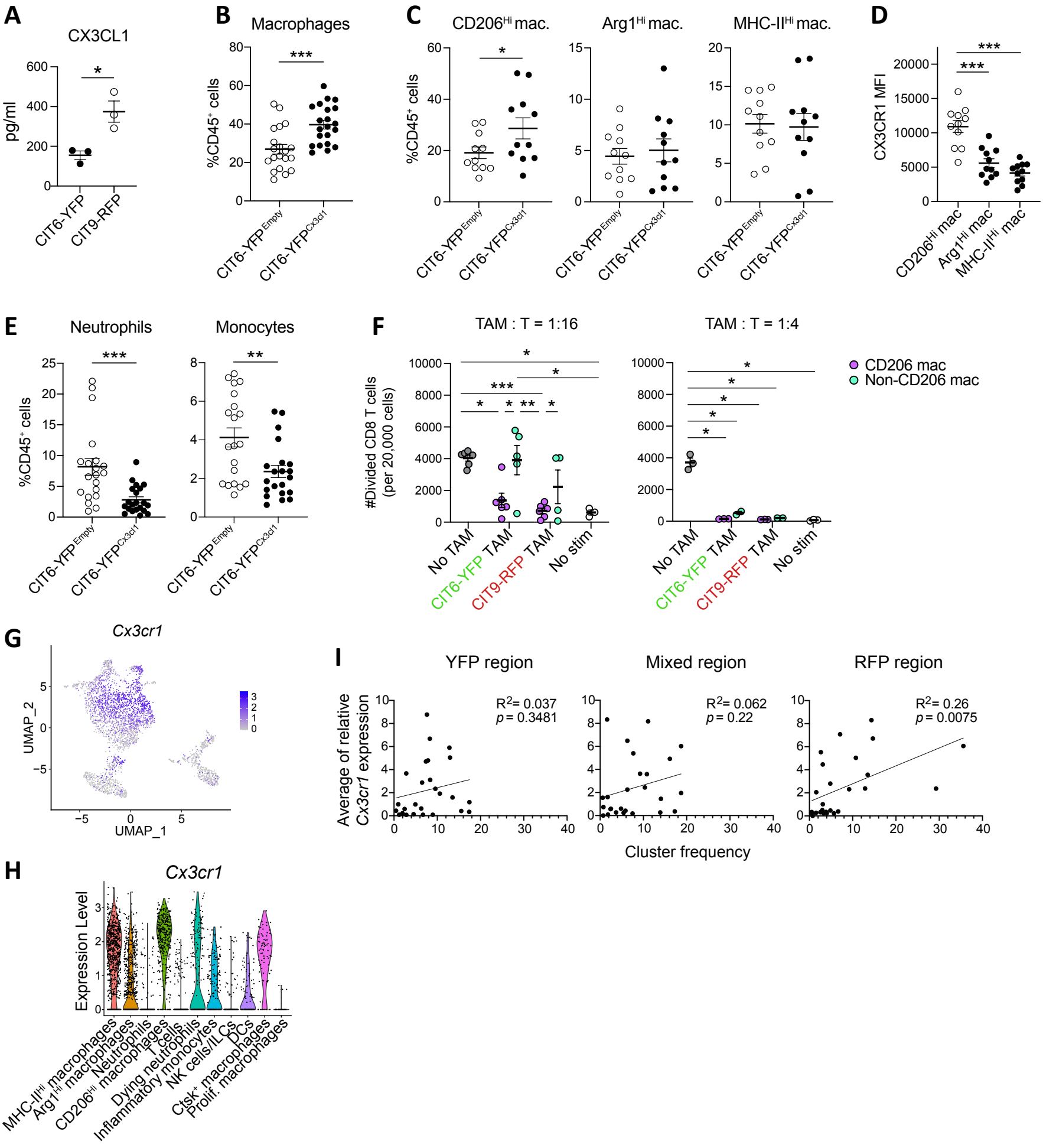
A
CX3CL1
pg/ml
CIT6-YFP
CIT9-RFP
B
Macrophages
%CD45⁺ cells
CIT6-YFP Empty
CIT6-YFP Cx3cr1
C
CD206Hi mac.
Arg1Hi mac.
MHC-IIHi mac.
D
CX3CR1 MFI
CD206Hi mac
Arg1Hi mac
MHC-IIHi mac
E
Neutrophils
Monocytes
F
TAM : T = 1:16
TAM : T = 1:4
#Divided CD8 T cells (per 20,000 cells)
No TAM
CIT6-YFP TAM
CIT9-RFP TAM
No stim
CD206 mac
Non-CD206 mac
G
Cx3cr1
UMAP_1
UMAP_2
I
YFP region
Mixed region
RFP region
Average of relative Cx3cr1 expression
R2= 0.037
p = 0.3481
R2= 0.062
p = 0.22
R2= 0.26
p = 0.0075
Cluster frequency
H
Cx3cr1
Expression Level
MHC-IIHi macrophages
Arg1Hi macrophages
Neutrophils
CD206Hi macrophages
T cells
Dying neutrophils
Inflammatory monocytes
NK cells/ILCs
DCs
Ctsk+ macrophages
Prolif. macrophages

Figure 6

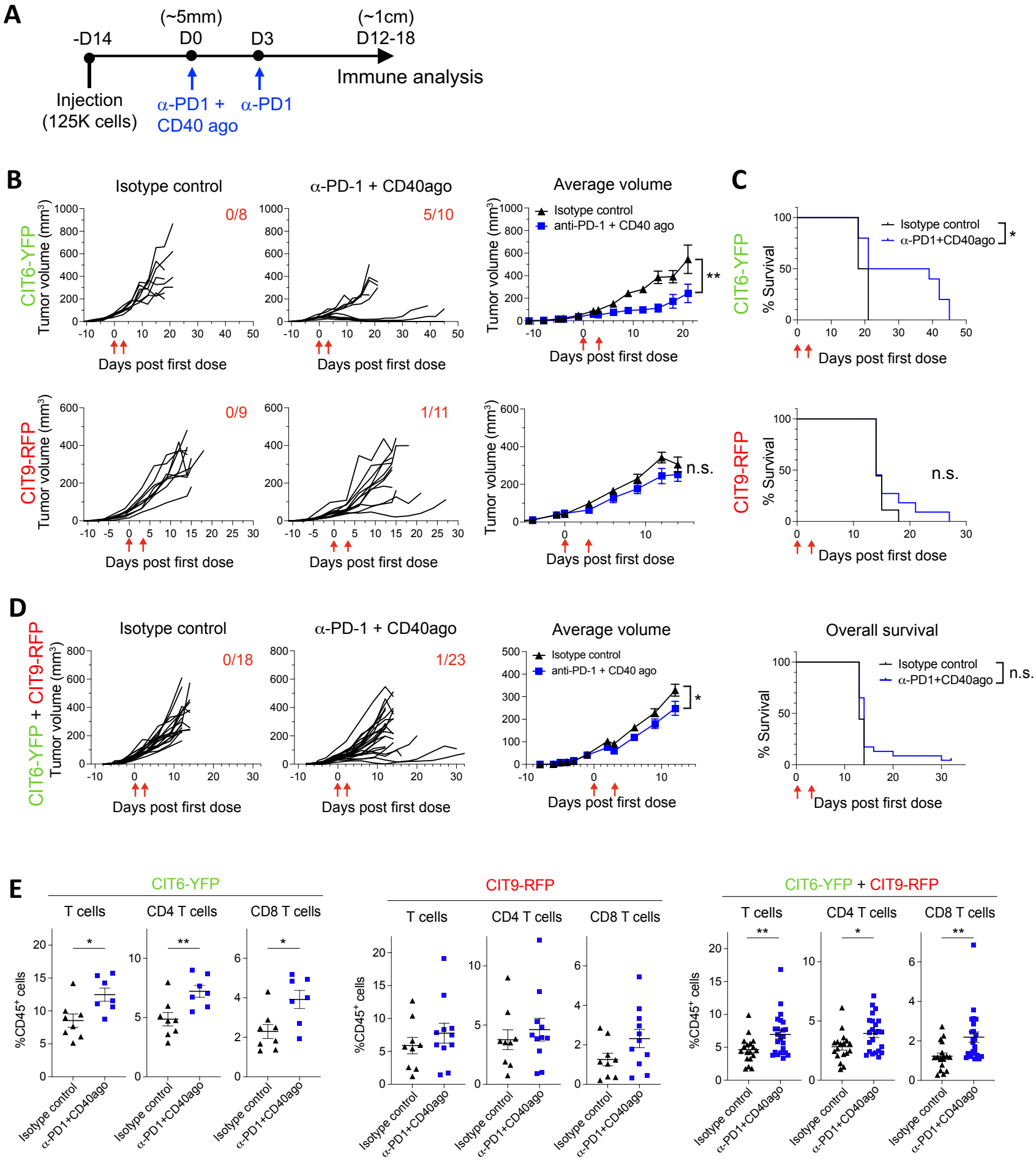
A
-D14
(~5mm)
D0
D3
(~1cm)
D12-18
Immune analysis
Injection
(125K cells)
α-PD1 +
CD40 ago
α-PD1
B
Isotype control
α-PD-1 + CD40ago
Average volume
CIT6-YFP
CIT9-RFP
Tumor volume (mm³)
Days post first dose
0/8
5/10
0/9
1/11
Isotype control
anti-PD-1 + CD40 ago
**
n.s.
C
% Survival
α-PD1+CD40ago
*
D
CIT6-YFP + CIT9-RFP
0/18
1/23
Overall survival
E
CIT6-YFP
CIT9-RFP
T cells
CD4 T cells
CD8 T cells
%CD45⁺ cells
Isotype control
α-PD1+CD40ago

Figure 7

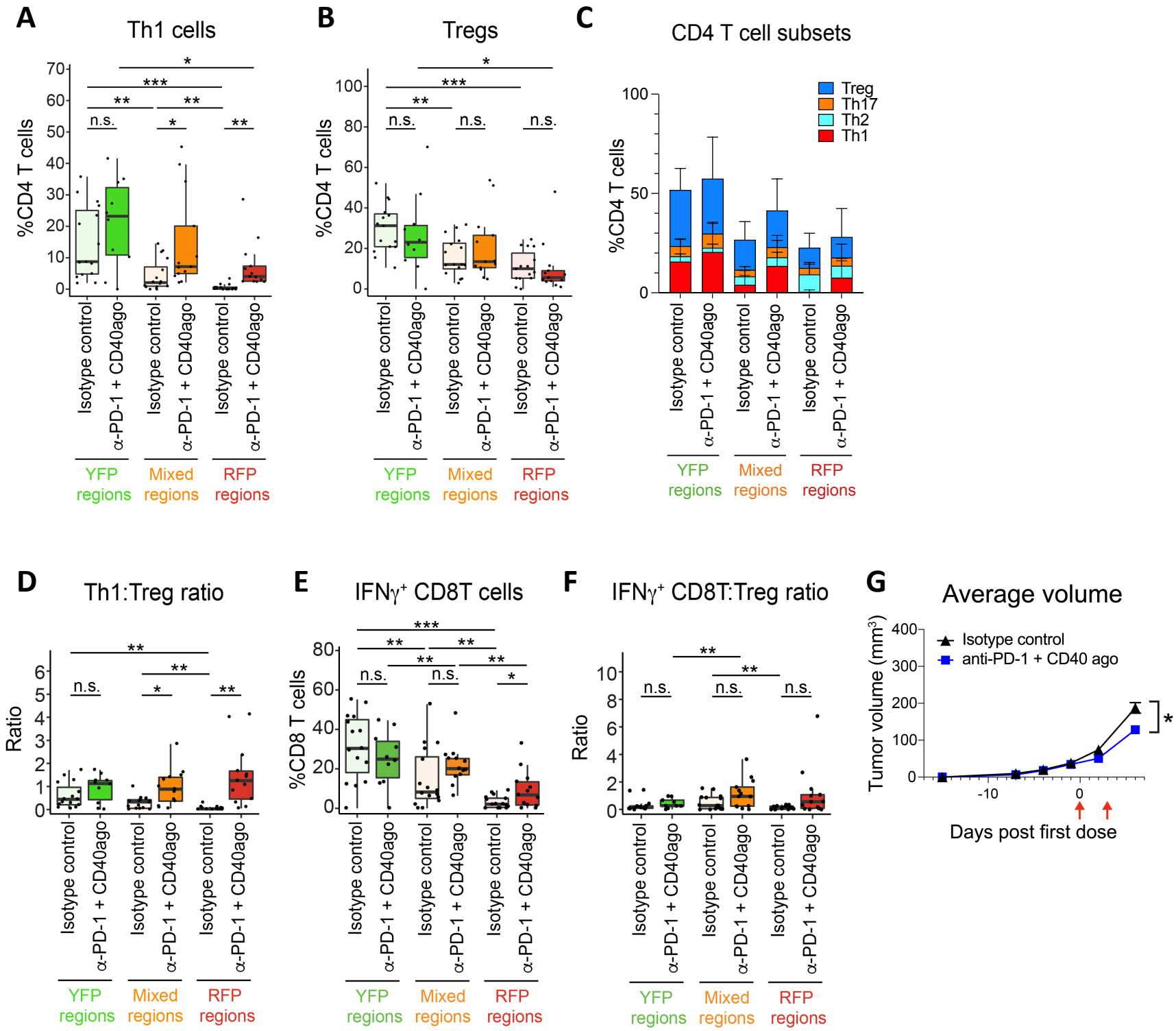
A
Th1 cells
%CD4 T cells
B
Tregs
%CD4 T cells
C
CD4 T cell subsets
%CD4 T cells
Treg
Th17
Th2
Th1
Isotype control
α-PD-1 + CD40ago
YFP regions
Mixed regions
RFP regions
D
Th1:Treg ratio
Ratio
E
IFNγ+ CD8T cells
%CD8 T cells
F
IFNγ+ CD8T:Treg ratio
Ratio
G
Average volume
Tumor volume (mm3)
Isotype control
anti-PD-1 + CD40 ago
Days post first dose